Investigation on Internal Flow Characteristics of a Pressure-Driven Swirling Injector for Urea-SCR System

Youcheng Shi[1(✉)], Zheng Li[1], Wenbin Cao[1], and Qingzhen Dong[2]

[1] College of Energy and Power Engineering, Lanzhou University of Technology, 287 Langongping Road, Lanzhou, China
shiyc@lut.edu.cn

[2] Ocean University of China, Qingdao, China

Abstract. A pressure-driven swirling injector for Urea-SCR system was presented and investigated. It consists of a switch valve and orifice. To investigate the dynamic and internal flow characteristics of the injector, a FSI model was proposed. Numerical analysis suggested that the flowrates of the injector under different inlet pressure were close to the test results. The deviations between the simulated and tested flowrate at different inlet pressure were less than 2%. It is demonstrated that the proposed simulation model was efficient to simulate a full working process of the injector. When the inlet pressure increased from 0.5 to 1.3 MPa, the discharge coefficients of the injector increased lightly. When the length-diameter ratio increased from 0.5 to 2.5, the discharge coefficients of the injector decreased lightly. When the eccentricity of swirl channel increased from 0.28 to 2.23, the discharge coefficients of the injector remained unchanged. The results showed that the inlet pressure and structural parameters of the injector have relatively little influence on the discharge coefficient. The results can provide a theoretical basis for the design of the similar injector.

Keywords: Urea injector · Internal flow · Pressure · Discharge coefficient · Urea selective catalytic reduction (Urea-SCR) system

1 Introduction

Urea selective catalytic reduction (Urea-SCR) technology is currently widely used in the exhaust aftertreatment of diesel engines [1–3]. The Urea-SCR technology adopts urea water solution (UWS) as the reducing agent to convert the NOx from the exhaust into N2 and H2O through a catalyst [4, 5]. Urea injector is one of core components of Urea-SCR system. Analyzing the dynamic characteristics of the injector and optimizing its structure, the performance of the Urea-SCR system can be effectively improved [6, 7].

Many authors have applied various methods and models to investigate the characteristics of the urea injectors [8–13]. Oha and Lee analyzed the motion characteristics of the nozzle using laser diagnostics and high-speed cameras to provide a reference for the

L. Yan and J. Na (Eds.): ICFPMCE 2022, AHE 10, pp. 376–392, 2023.
https://doi.org/10.2991/978-94-6463-022-0_32

optimal distance from the mixer to the urea injector. The droplet uniformity index (DUI) was calculated from the test data to obtain the spray droplet distribution. The results proved that the grid-channel plate-type mixer is better than the case without a mixer, which DUI could increase 32% [8]. Varna et al. found that two counter-rotating kidney vortices are formed at low cross-flow conditions and can improve mixing. Under the condition of higher flow velocity, the vortex is not formed obviously, and the interaction between the spray wall is not obvious [9].

Some other researchers are mainly focused on the spray characteristics of the injectors and atomization process of UWS. Hua et al. used high-speed photography investigated the urea spray characteristics of two typical urea injectors (air-assisted and non-air-assisted) at normal temperature and pressure. For the SCR system without air assistance, the injection (pressure-driven type) rate shows basically no effects on urea spray pattern. The droplet size in SCR injection system with air assistance is much smaller compared with that in SCR injection system without air assistance [10]. Spiteri et al. conducted experiments on two commercial UWS injectors to obtain spray characteristics under different cross-flow conditions. Experimental results show that the extensive volume fraction in the largest droplets can affect the distribution of urea under pressure driving. Turbulence and vorticity caused by the ejector airflow can affect the distribution of smaller droplets in air-assisted atomization [11]. Shi et al. conducted experimental studies on non-air-assisted ejectors and found that when the ejection pressure was reasonable, the spray formed without impinging the wall. The lower injection pressure led to better axial concentration uniformity of the urea-solution droplet distribution. The decrease of injection pressure resulted in mixing distance decrease [12].

As the reliability of the non-air-assisted systems is far higher than the air-assisted systems. The non-air-assisted SCR system will be the main products in the future. Lee and Park studied internal flow characteristics of two types of commercial pressure-driven injectors. The average discharge coefficient of the H-type injector is 0.59, and that of the D-type injector was 0.53. The H-type injector has better UWS supply characteristics and could reach stable flow conditions faster than the D-type injector [13]. The research results of Postrioti et al. suggested that back-light imaging (BLI) can be a good choose in those cases when the use of phase Doppler anemometry is limited by geometry [14]. Shahariar and Lim conducted experiments on spray and droplets of a pressure-driven SCR injector, applying Z-Shadow imaging to capture spray images, and UWS spray, droplet disintegration, urea disintegration, and deposit formation for SCR systems were analyzed. The study revealed that higher pressure increases the ratio of wall impingement and deposit formation. The droplet size mainly depended on injection pressure, and exhaust temperature also had significant influences on droplet size and evaporation [15]. Payri et al. investigated the atomization of UWS by optical diagnosis through BLI. The results showed that the atomization process of UWS solution is related to the injection pressure. Increasing the injection pressure will increase the atomization speed, generate smaller droplets, make the spray angle wider, and improve the evaporation and mixing performance of the SCR system [16].

The dynamic characteristics of solenoid valve of pressure-driven injector were also investigated by some researchers. Wang et al. studied the response time of the solenoid valve of a pressure-driven injector. The results showed that, in a certain range, changing air gap and spring stiffness could produce the opposite effect on opening and closing time. The number of coil turns and the coil resistance could produce greater influence on closing time [17]. There are three or more orifices (nearly 0.18 mm) in most of the pressure-driven injectors. If the swirling injector is adopted in SCR system, the diameter of the orifice can reach 0.28 mm. Obviously, the pressure-driven swirling injector has lower cost than the other type. However, few studies focus on the pressure-driven swirling injectors for Urea-SCR system.

In this paper, a pressure-driven swirling injector for the Urea-SCR system is presented. The main goal of this work is to establish a three-dimensional FSI model of the ejector, and based on this model, the dynamic characteristics and internal flow characteristics of the ejector are analyzed. And the control experiment of the prototype injector is performed out in this paper, and the results show that the test results are close to those of the established simulation model. Based on the proposed model, the dynamic characteristics and internal flow characteristics of the injector are investigated.

2 Theoretical Methods

The proposed simulation model of the injector contains fluid filed and structure field.

2.1 Injector Configuration

The configuration of the pressure-driven swirling injector is presented in Fig. 1.

It consists of a switch valve and orifice. The switch valve consists of valve seat, valve core, shell, spring, iron core, coils, and magnet yoke, and so on. The valve core is also the armature. When the coil is not energized, the switch close and UWS cannot spray out through the injector. When the coil is energized, the armature moves upward and the UWS can spray out through the injector. Some parameters of the injector list in Table 1.

The movement of the valve core will affect the flow of the UWS, and the UWS also has a mechanical effect on the valve core. The FSI model is established to study the movement characteristics of the injector and the flow of the UWS. In FSI calculation, the fluid model and solid model are respectively defined based on their material data, structure parameters, boundary conditions, and so on.

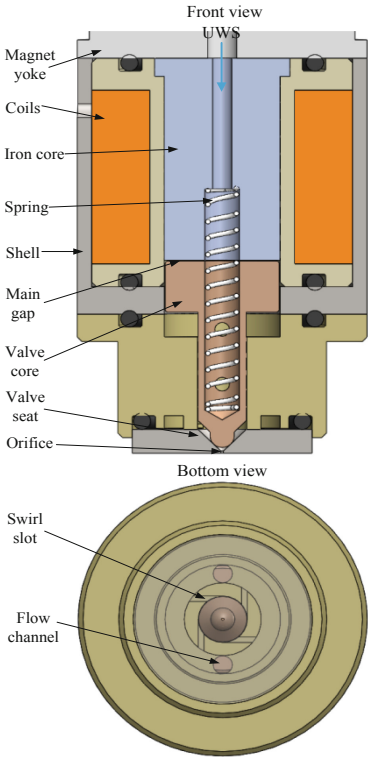

Fig. 1. Configuration of the pressure-driven swirling injector.

Table 1. Parameters of the pressure-driven swirling injector

Symbol	Parameter	Value
p	Rated pressure	0.9 MPa
f_o	Operating frequency	1 Hz
Q	Rated flow rate	7.0 L/h
g_a	Main gap	0.1 mm
d_o	Diameter of orifice	0.28 mm
l_0	Length of orifice	0.25 mm
d_v	Diameter of valve	2.5 mm
θ	Valve seat cone angle	90°
n	Number of swirl channel	4
e_s	Eccentricity of swirl channel	2.2 mm

2.2 Fluid Part

2.2.1 Theoretical Foundation

The governing equation of fluid motion can be given as follow,

$$\frac{\partial \rho}{\partial t} + \nabla \cdot (\rho \mathbf{V}) = 0 \tag{1}$$

$$\frac{\partial \rho \mathbf{V}}{\partial t} + \nabla \cdot (\rho \mathbf{V}\mathbf{V} - \boldsymbol{\tau}) = \mathbf{f}_b \tag{2}$$

$$\frac{\partial \rho E}{\partial t} + \nabla \cdot (\rho \mathbf{V} E - \boldsymbol{\tau} \cdot \mathbf{V} + \mathbf{q}) = \mathbf{f}_b \cdot \mathbf{V} + q_b \tag{3}$$

where ρ is the density, $\boldsymbol{V}$ is the velocity vector, t is the time, $\boldsymbol{\tau}$ is the stress tensor, $\boldsymbol{f}_b$ is the vector of body force, E is the specific total energy, $\boldsymbol{q}$ is the heat flux and q_b is the specific rate of heat generation [18].

2.2.2 Mesh Model and Boundary Conditions

It is critical to ensure grid nodal coincidence between two adjacent bodies to conduct the FSI simulation. To simulate the displacement of the valve core, the moving mesh technology is needed. If the triangular grid is adopted, it will greatly increase the number of grid cells and computational expense. As a result, a mesh model with high-quality hexahedral grids is created. The fluid model with hexahedral cells presents in Fig. 2. Elements in fluid model are 3D 8-node cells.

The fluid model is calculated using the Spalart-Allmaras (S-A) turbulence model. The S-A model is appropriate for simulating this type of problem, it has been used and verified by some researchers to complete similar works [19–22].

The switch valve is periodically opened and closed, so it can be simulated using the GAP boundary condition (GAPBC). In the initial state of the fluid domain grid, a gap of 0.002 mm needs to be set between the valve core and the valve seat, it is shown in Fig. 3. GAPBCs are applied on the specified interfaces between two adjacent fluid fields. The GAPBC is a switch which can control the flow condition of fluid. When the switch is opening, the fluid in two fields is connected across the interfaces and the fluid variables are continuous. When the switch is closing, the fluid in two fields is not connected and variables are discontinuous. The red arrow in Fig. 3 represents the flow direction of UWS. Boundary condition of fluid structure interface (BCFSI) is applied on all faces which adjacent to structure domain. The inlet and outlet face of fluid domain are governed by pressure boundary condition.

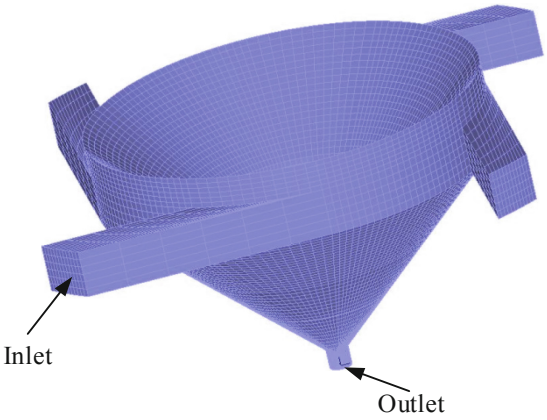

Fig. 2. Fluid domain.

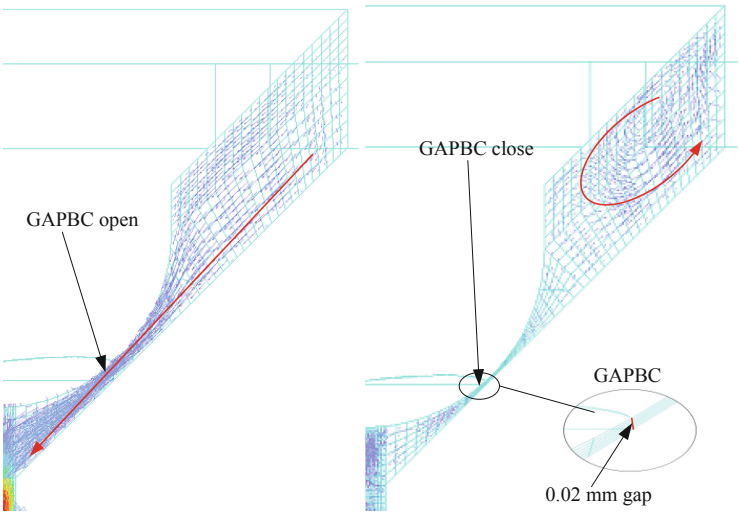

Fig. 3. GAPBC of the switch valve.

2.3 Structure Part

2.3.1 Theoretical Foundation

In analysis of structure model, the equilibrium equations can be expressed as follows,

$$\boldsymbol{M\ddot{U} + C\dot{U} + KU = R - F} \tag{4}$$

where M is the mass matrix, U is the displacement vector, $\boldsymbol{C}$ is the damping matrix, K is the stiffness matrix, $\boldsymbol{R}$ is the external load, $\boldsymbol{F}$ is the force vector of nodal point.

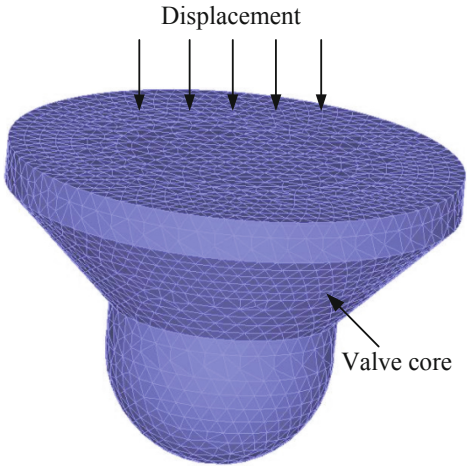

Fig. 4. Structure domain.

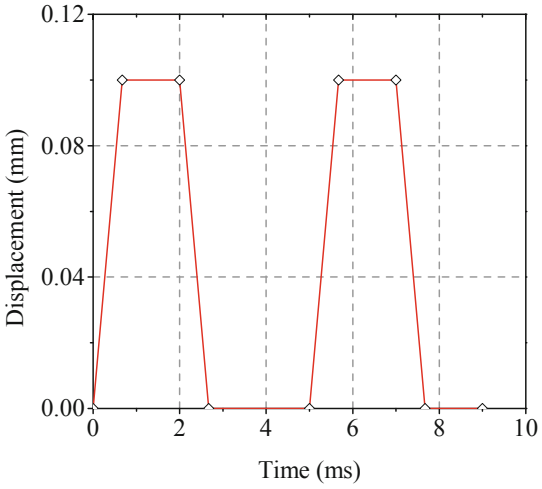

Fig. 5. Function of the valve core displacement.

2.3.2 Mesh Model and Boundary Conditions

The mesh model of the structure field is presented in Fig. 4. Cells in this model are 3D 4-node elements. The motion of the valve core is governed by a function, and it is showed in Fig. 5. The BCFSI is also applied on all faces which adjacent to fluid domain.

The valve core is made of perm alloy. Water is used to replace UWS to conduct the simulation and experiment. The parameters of the simulation model are set as shown in Table 2.

Table 2. Setting Parameters of the simulation model

Parameter	Value
Elasticity modulus of perm alloy (GPa)	200
Passion's ratio of steel	0.3
Bulk modulus of water (GPa)	2.2
Dynamic viscosity of water (Pa · s)	1×10^{-3}
Density of water (kg/m^3)	1000
Time step (s)	5×10^{-6}

2.4 FSI Model

The governing equation of the BCFSI can be expressed as follows,

$$\mathbf{d}_f = \mathbf{d}_s \tag{5}$$

$$\mathbf{n} \cdot \boldsymbol{\tau}_f = \mathbf{n} \cdot \boldsymbol{\tau}_s \tag{6}$$

$$\mathbf{V} = \dot{\mathbf{d}}_s \tag{7}$$

where $\boldsymbol{d}_f$ is the displacement of fluid, $\boldsymbol{d}_s$ is the displacement of solid, $\boldsymbol{\tau}_f$ is the fluid stress, $\boldsymbol{\tau}_s$ is solid stress.

Obviously, the displacement of fluid nodes on the BCFSI can be worked out based on the above equations, and then the other fluid nodal points can be calculated automatically by program. The velocities of fluid nodes on the BCFSI are zero.

The fluid tractions are integrated into force vectors along the BCFSI and applied onto the structure nodes. The equation can be expressed as follow,

$$\mathbf{F}(t) = \int h \cdot \boldsymbol{\tau}_f dS \tag{8}$$

where h is the virtual quantity of the solid displacement [18].

The fluid and structure models are solved by the same one FSI solver. To work out the coupling system, the iterative computing methods are adopted. Figure 6 presents the flow chart of the FSI calculation. The initial value is $\boldsymbol{\tau}_{\mathrm{s}}^{0} = {}^{t}\boldsymbol{\tau}_{\mathrm{s}}$ and $\boldsymbol{d}_{\mathrm{s}}^{-1} = \boldsymbol{d}_{\mathrm{s}}^{0} = {}^{t}\boldsymbol{d}_{\mathrm{s}}$.

2.5 Mesh Sensitivity

Six simulation models with different grid numbers are built and calculated. The jet flowrate presents in Table 3. Clearly, when the number of grid cells exceed 97 200 it can only make the results stable. To make the best compromise between the computational cost and precision, the selected simulation model consists of 97 200 grid cells.

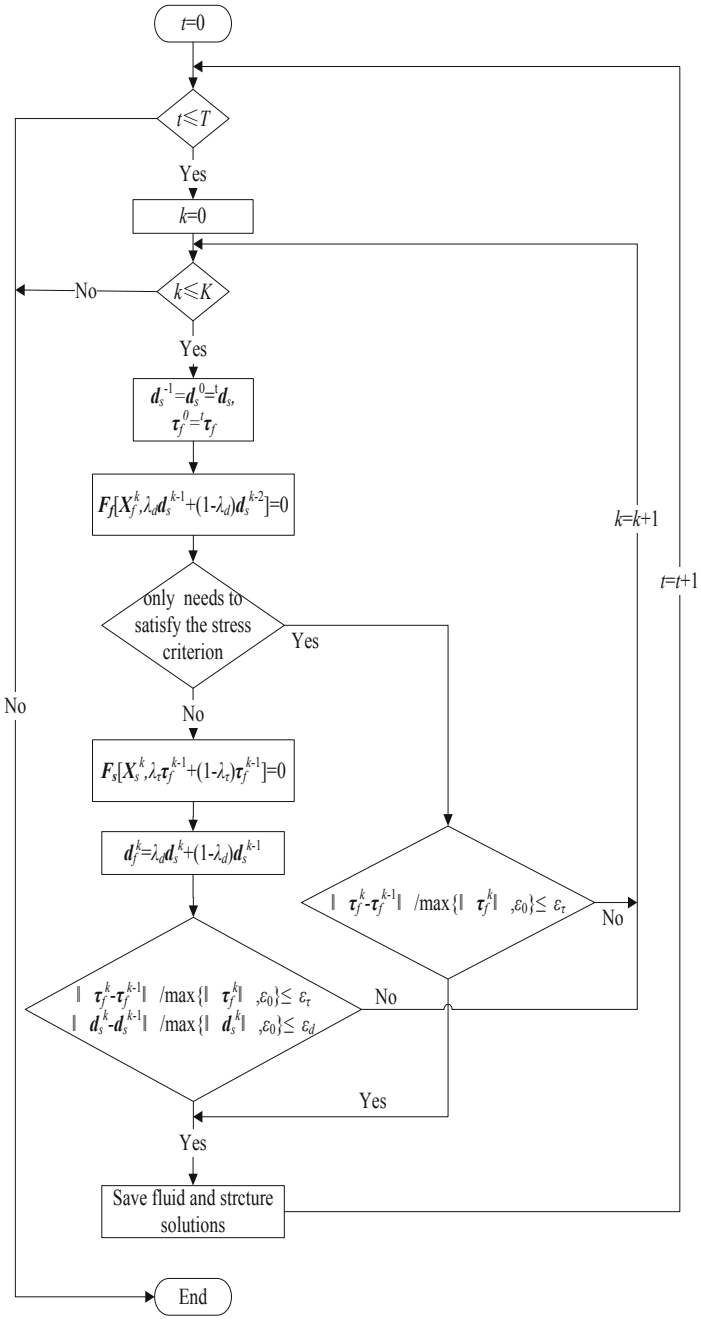

Fig. 6. Flow chart of the FSI calculation.

Table 3. The results of mesh sensitivity analysis

Item	Mesh number (10^4)		Mass flowrate (L/h)
	Fluid domain	Structure domain	
Test 1	5.83	2.81	6.87
Test 2	5.83	3.94	6.95
Test 3	6.91	2.81	7.01
Test 4	6.91	3.94	7.01
Test 5	7.76	2.81	7.01
Test 6	7.76	3.94	7.01

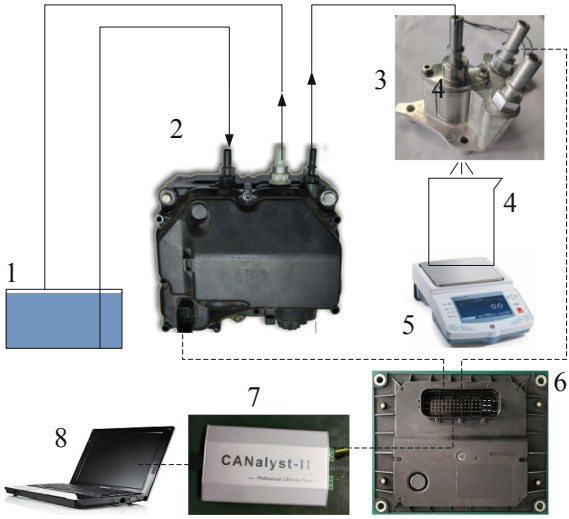

1-tank 2-Urea pump 3-prototype of injector 4-measuring cup
5-electronic scale 6-DCU 7-CANalyst 8-monitor

Fig. 7. Component photos of the test system.

3 Experiments

To verify the simulation model, a injector and test system are fabricated. Figure 7 shows the component photos of the test system. The arrows represents the flow direction of fluid. Table 4 lists the parameters of the test rig components. The flowrates of injector are measured by the weighting method.

Table 4. Parameters of the components of the test system

Range of electronic scale (g)	0–5000
Resolution of electronic scale (g)	0.01

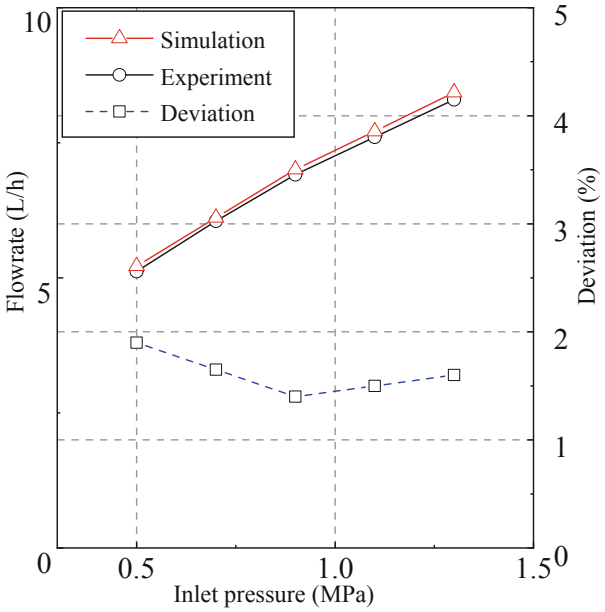

Fig. 8. Relationship between the inlet pressure and injector flowrate.

4 Results and Discussions

4.1 Validation of the Simulation Model

The flowrate of the injector under different inlet pressure is calculated. The simulation results and experiment results are presented in Fig. 8. When the pressure changed from 0.5 to 1.3 MPa, the two flowrates are all proportional to the inlet pressure. The deviations between the two flowrates under different conditions are less than 2%. The results show that the simulation model is efficient.

4.2 Internal Flow of Injector

The pressure and velocity are important parameters to describe the internal flow characteristics of the injector. The total pressure and velocity contours in internal flow domain of injector are showed in Fig. 9.

At 5.02 ms, the valve is opening, and the pressure drop across GAPBC is nearly 0.1 MPa. At 6.22 ms, the valve is open and the maximum velocity at outlet is nearly

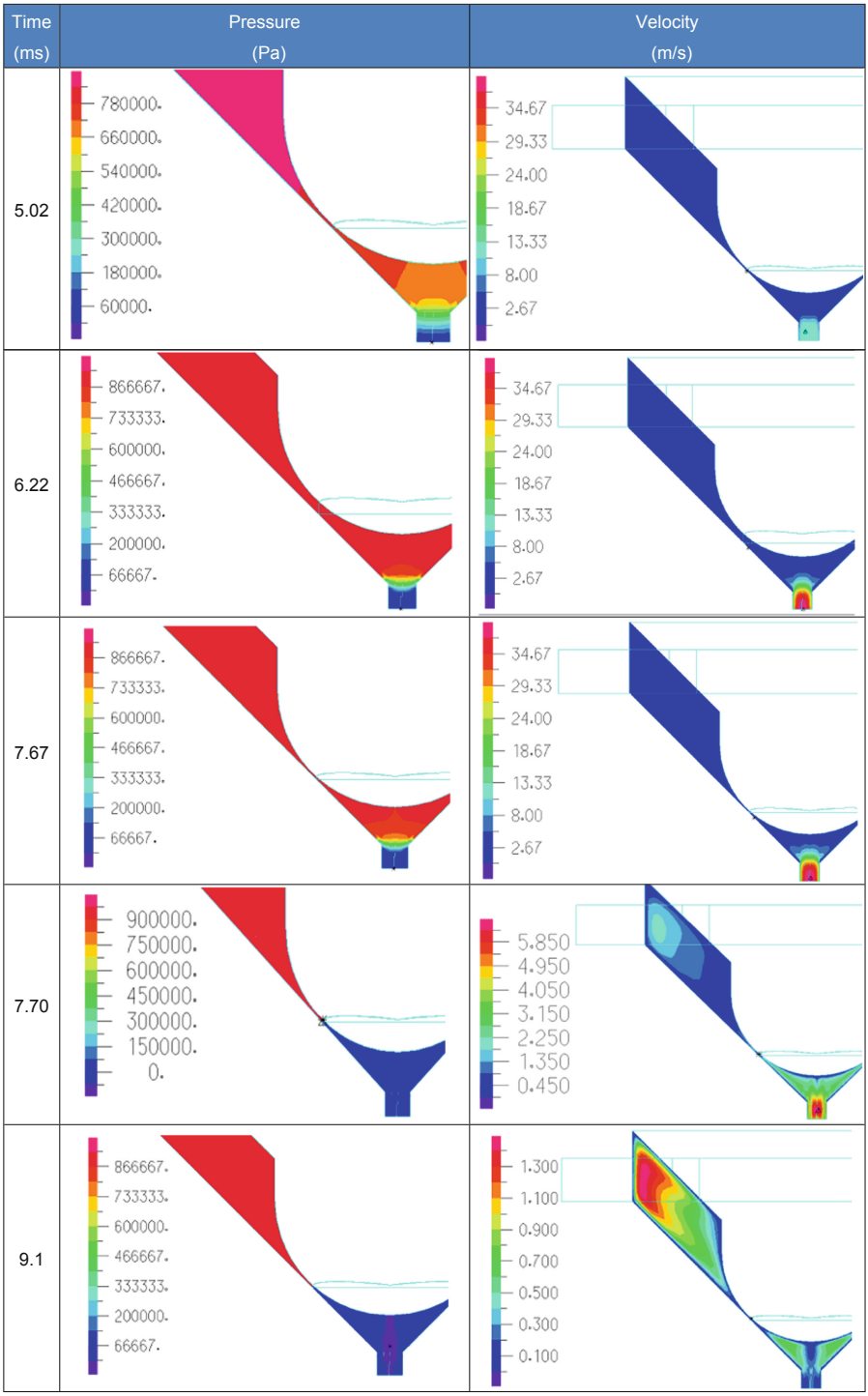

Fig. 9. Total pressure and velocity contours of the injector.

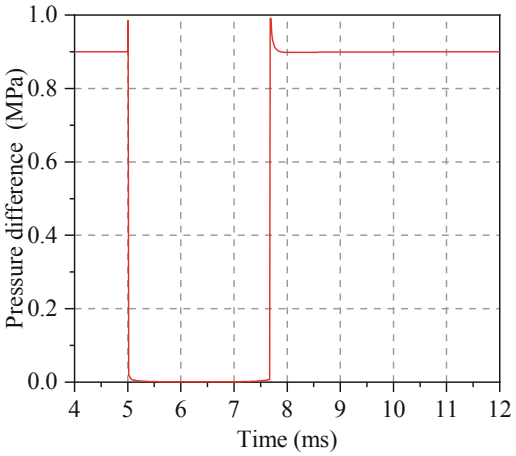

Fig. 10. Pressure differences between the inlet port and outlet port.

39 m/s. At 7.67 ms, the valve will close, and the minimum velocity is at valve port. At 7.70 ms, the valve is close and negative pressure is produced at valve port. The fluid at outlet continues to flow out. At 9.1 ms, the valve is close and the fluid at outlet nearly stops flowing.

The pressure difference between the inlet and outlet port is shown in Fig. 10. When the valve is open, the pressure difference is nearly 0. When the valve is close, the pressure difference is nearly 0.9 MPa. At 5.01 and 7.68–7.8 ms, the pressure differences are larger than 0.9 MPa. In the start of opening process and end of closing process, negative pressure is produced at valve port and the vacuum is nearly 0.1 MPa. That means cavitation may occur at the valve port. This phenomenon is harmful to injector.

4.3 Discharge Coefficient of the Injector

The flowrate of the injector can be calculated as follow,

$$Q = C_{\mathrm{d}} A \sqrt{\frac{2\Delta p}{\rho}} \tag{9}$$

where C_{d} is the discharge coefficient, Δp is the pressure drop across the orifice, A is the cross-sectional area.

The discharge coefficients of the injector under different conditions are showed in Fig. 11. When the inlet pressure increases from 0.5 to 1.3 MPa, the discharge coefficients of the injector increase lightly. When the $l_{\mathrm{o}}/d_{\mathrm{o}}$ increases from 0.5 to 2.5, the discharge coefficients of the injector decrease lightly. When the e_{s} increases from 0.28 to 2.23, the discharge coefficients of the injector unchanged. The results showed that the $l_{\mathrm{o}}/d_{\mathrm{o}}$ is the main effect influenced the discharge coefficient.

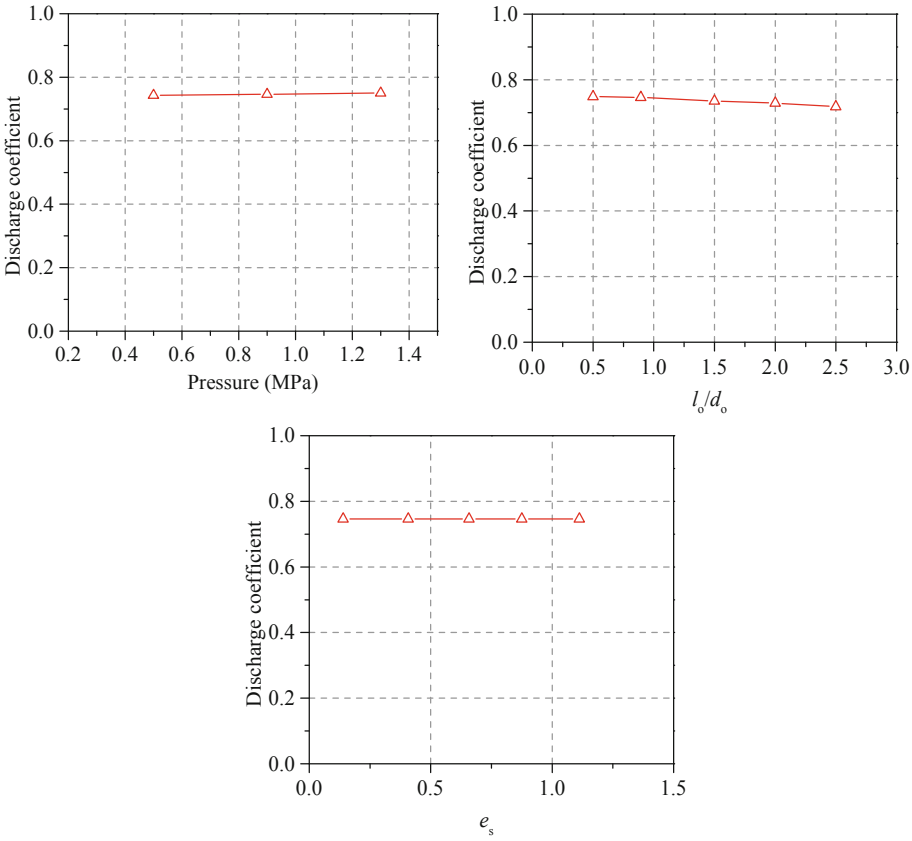

Fig. 11. Discharge coefficient of the injector under different conditions.

5 Conclusions

A pressure-driven swirling injector was presented and investigated. It consists of a switch valve and orifice. To investigate the dynamic and internal flow characteristics of the injector, a FSI model was built. A prototype injector was manufactured and tested.

Simulation results suggested that the flowrates of the injector under different inlet pressure are close to the test results. The deviations between two flowrates under different inlet pressure were less than 2%. The test results show that the FSI model established above can effectively simulate the kinematic characteristics and internal flow of the injector. When the inlet pressure increased from 0.5 to 1.3 MPa, the discharge coefficients of the injector increased lightly. When the lo/do increased from 0.5 to 2.5, the discharge coefficients of the injector decreased lightly. When the es increased from 0.28 to 2.23, the discharge coefficients of the injector remained unchanged. The results showed that the lo/do is the main effect influenced the discharge coefficient. The results will provide a theoretical basis for the design of the similar injector.

Acknowledgement. Project supported by the Natural Science Foundation of Gansu Province, China (Grant No. 21JR7RA270).

Appendix 1

Notation

p: Rated pressure
f_o: Operating frequency
Q: Rated flow rate
g_a: Main gap
d_o: Diameter of orifice
l_0: Length of orifice
n: Number of swirl channel
d_v: Diameter of valve
θ: Valve seat cone angle
e_s: Eccentricity of swirl channel
C: damping matrix
d_s: solid displacement
d_f: fluid displacement
F: force vector of nodal point
E: specific total energy
f_b: vector of body force
K: stiffness matrix
M: mass matrix
q_b: specific rate of heat generation
q: heat flux
R: external load vector
t: time (s)
U: displacement vector
ρ: density (kg/m^3)
V: velocity vector of fluid
τ stress tensor
τ_s: solid stress
τ_f: fluid stress

References

1. Koebel, M., Elsener, M., Kleemann, M.: Urea-SCR: a promising technique to reduce NOx emissions from automotive diesel engines. Catal. Today **59**, 335–345 (2000). https://doi.org/10.1016/s0920-5861(00)00299-6
2. Johnson, T., Joshi, A.: Review of vehicle engine efficiency and emissions. SAE Int. J. Engines **11**, 1307–1330 (2018). https://doi.org/10.4271/2019-01-0314

3. Johnson, T.V.: Review of Selective Catalytic Reduction (SCR) and Related Technologies for Mobile Applications. 'Urea-SCR Technology for deNOx After Treatment of Diesel Exhausts'. Springer, New York (2014). https://doi.org/10.1007/978-1-4899-8071-7-1
4. Assadian, F., Abapo, G., Beckerman, A.: Modeling of selective catalytic reduction injection system using bond graphs for real time. In: Proceedings of the International Conference on Bond Graph Modeling and Simulation, pp. 169–180 (2016). https://doi.org/10.22360/summersim.2016.icbgm.019
5. Janssens, T.V.W., Falsig, H., Lundegaard, L.F., et al.: A consistent reaction scheme for the selective catalytic reduction of nitrogen oxides with ammonia. ACS Catal. **5**(5), 2832–2845 (2015). https://doi.org/10.1021/cs501673g
6. Jeong, S.J., Lee, S.J., Kim, W.S.: Numerical study on the optimum injection of urea–water solution for SCR DeNOx system of a heavy-duty diesel engine to improve DeNOx performance and reduce NH3 slip. Environ. Eng. Sci. **25**(7), 1017–1036 (2008). https://doi.org/10.1089/ees.2007.0224
7. Qi, Z., Li, S., Guo, X.: Development, application and direction of development of Urea-SCR. Int. J. Multimedia and Ubiquitous Eng. **11**(6), 131–142 (2016). https://doi.org/10.14257/ijmue.2016.11.6.12
8. Oh, J., Lee, K.: Spray characteristics of a urea solution injector and optimal mixer location to improve droplet uniformity and NOx conversion efficiency for selective catalytic reduction. Fuel **119**, 90–97 (2014). https://doi.org/10.1016/j.fuel.2013.11.032
9. Varna, A., Spiteri, A.C., Wright, Y.M., et al.: Experimental and numerical assessment of impingement and mixing of urea–water sprays for nitric oxide reduction in Diesel exhaust. Appl. Energy **157**, 824–837 (2015). https://doi.org/10.1016/j.apenergy.2015.03.015
10. Hua, L., Zhao, Y.G., Hu, J., et al.: A comparative experimental study on the urea spray characteristics in SCR Systems w/wo air assistance. Automot. Eng. **35**, 197–201 (2013)
11. Spiteri, A., Eggenschwiler, P.D., Liao, Y., et al.: Comparative analysis on the performance of pressure and air-assisted urea injection for selective catalytic reduction of NOx. Fuel **161**, 269–277 (2015). https://doi.org/10.1016/j.fuel.2015.08.061
12. Shi, X., Deng, J., Wu, Z., et al.: Effect of injection parameters on spray characteristics of urea-SCR system. SAE Int. J. Engines **6**(2), 873–881 (2013). https://doi.org/10.4271/2013-01-1067
13. Lee, S.I., Park, S.Y.: Numerical analysis of internal flow characteristics of urea injectors for SCR dosing system. Fuel **129**, 54–60 (2014). https://doi.org/10.1016/j.fuel.2014.03.031
14. Postrioti, L., Brizi, G., Ungaro, C., et al.: A methodology to investigate the behavior of urea-water sprays in high temperature air flow for SCR de-NOx applications. Fuel **150**, 548–557. https://doi.org/10.1016/j.fuel.2015.02.067
15. Shahariar, G.M.H., Lim, O.T.: Investigation of urea aqueous solution injection, droplet breakup and urea decomposition of selective catalytic reduction systems. J. Mech. Sci. Technol. **32**(7), 3473–3481 (2018). https://doi.org/10.1007/s12206-018-0651-5
16. Payri, R., Bracho, G., Gimeno, J., et al.: Investigation of the urea-water solution atomization process in engine exhaust-like conditions. Exp. Thermal Fluid Sci. **108**, 75–84 (2019). https://doi.org/10.1016/j.expthermflusci.2019.05.019
17. Wang, Q., Lai, X., Hu, J., et al.: Simulation analysis of the non air assisted SCR urea nozzles solenoid valve based on ansoft. Chin. J. Automot. Eng. **7**(1), 873–881 (2017)
18. Ynamic, U., Onlinear, N.: Theory and Modeling Guide Theory and Modeling Guide: Volume III: CFD & FSI. ADINA R&D, Inc, Watertown (2017)
19. Spalart, P.R., Allmaras, S.R., Reno, J.: A one-equation turbulence model for aerodynamic flows. In: 30th Aerospace Sciences Meeting and Exhibit, Reno, NV, 6–9 January 1992, pp. 1–10. AIAA, New York. https://doi.org/10.2514/6.1992-439

20. Allmaras, S.R., Johnson, F.T., Spalart, P.R.: Modifications and clarifications for the implementation of the Spalart-Allmaras turbulence model. In: Seventh International Conference on Computational Fluid Dynamics, Big Island, Hawaii, 9–13 July 2012, pp. 1–11. ICCFD, New York
21. Ling, X., Zhang, W., Chen, Y.: Numerical simulation of suction valve internal flow field of large scale diaphragm pump fluid end based on ADINA. Adv. Mater. Res. **706**, 1458–1461 (2013). https://doi.org/10.4028/www.scientific.net/amr.706708.1458
22. Zeng, Y., Liu, X.: Simulation on blade duct vortex in a Francis turbine runner based on S-A model. Adv. Mater. Res. **444**, 476–478 (2014). https://doi.org/10.4028/www.scientific.net/amm.444445.476